

Tunable exciton polaritons in band-gap engineered hexagonal boron nitride

Pedro Ninhos ¹, Christos Tserkezis ¹, N. Asger Mortensen ^{1,2} and Nuno M. R. Peres ^{1,3,4}

¹*POLIMA—Center for Polariton-driven Light–Matter Interactions,*

University of Southern Denmark, Campusvej 55, DK-5230 Odense M, Denmark

²*Danish Institute for Advanced Study, University of Southern Denmark, Campusvej 55, DK-5230 Odense M, Denmark*

³*Centro de Física (CF-UM-UP) and Departamento de Física,*

Universidade do Minho, P-4710-057 Braga, Portugal

⁴*International Iberian Nanotechnology Laboratory (INL),*

Av Mestre José Veiga, 4715-330 Braga, Portugal

We show that hexagonal boron nitride (hBN), a two-dimensional insulator, when subjected to an external superlattice potential forms a new paradigm for electrostatically tunable excitons in the near- and mid-ultraviolet (UV). The imposed potential has three consequences: (i) it renormalizes the effective mass tensor, leading to anisotropic effective masses; (ii) it renormalizes the band gap, eventually reducing it; (iii) it reduces the exciton binding energies. All these consequences depend on a single dimensionless parameter, which includes the product of strength of the external potential with its period. In addition to the excitonic energy levels, we compute the optical conductivity along two orthogonal directions, and from it the absorption spectrum. The results for the latter show that our system is able to mimic a grid polarizer. These characteristics make one-dimensional hBN superlattices a viable and unexplored platform for fine-tuned polaritonics in the UV to visible spectral range.

I. INTRODUCTION

The properties of two-dimensional (2D) materials are characterized by a richness of physical phenomena, encompassing unusual elastic [1], electronic [2], and optical properties [3]. An exemplary case of enhanced light–matter interactions in 2D materials is provided by graphene [4], whose transmission in the visible range of the spectrum is characterized by the value of the fine structure constant alone, a unique case in materials. Concerning the electronic properties in 2D materials, we can find semi-metals [5], conductors [6], semi-conductors and insulators [7, 8], strange metals [9], metallic ferromagnets [10, 11], and superconductors [12–15]. Therefore, 2D materials have become a condensed-matter physicist’s playground due to this wealth of physical properties. Some systems, such as hexagonal boron nitride (hBN), have an interesting story: its first application was as an encapsulating medium for graphene and other 2D materials, due to its ultra-flat surface and low density of defects [16]. Such use allows to increase the mobility of charge carriers [17] and produce well defined (large quality factor Q) electromagnetic (EM) resonances in polaritonic devices. Later, it became clear that hBN is interesting in its own right when light–matter interaction is considered [18, 19]. The interaction with infrared radiation due to polar phonons in hBN gives rise to large- Q polaritonic resonances used for example in gas sensing [20]. At the same time, the interaction of ultraviolet (UV) radiation with the electrons in hBN has opened the field of UV photonics [21].

2D materials can be combined by stacking several layers, forming van der Waals heterostructures; materials consisting of few layers have proven to be a fertile theoretical and experimental playground for the study of unconventional physics [22]. On one hand, heterostruc-

tures are promising for tailoring optoelectronic properties of 2D insulators (such as hBN) [18]. On the other hand, homostructures reveal quite interesting features, distinct from those of the initial isolated constituents. From the example of AB-stacking graphene bilayer, it was realized that a band gap can be opened and controlled electrostatically, using a voltage bias [23, 24]. In twisted bilayer graphene, it was observed that a superlattice potential has a tremendous impact on the electronic and optical properties of 2D materials [25–27]. Armed with this information, it is possible to envision a combination of both electrostatic and superlattice potentials such that the electronic and optical properties of 2D materials can be externally controlled. One can manipulate the electronic and optical properties of a material by band-gap engineering [28]. For example, it is possible to change the gap of bulk hBN by femtosecond laser pulses [29]. For monolayer hBN, the band gap can be reduced by cladding the hBN between two graphene layers [30], or by functionalization [31].

In this context, it is pertinent to ask if one can manipulate the physical properties of hBN, the 2D material considered in this work, by forming a superlattice, resulting from combining a hBN lattice with an electrostatic periodic potential [Fig. 1(a)]. As a pristine 2D lattice, hBN is a wide band gap insulator in which boron (B) and nitrogen (N) atoms are arranged in a honeycomb lattice, bounded by strong covalent bonds. Unlike graphene, hBN presents a large band gap at the K and K’-points of the Brillouin zone (BZ) [see Fig. 1(b)], and the low-energy dispersion is quadratic and not linear, as it is in graphene. In a recent work [32], a direct measurement of the density of states of monolayer hBN by scanning tunneling microscopy revealed a band gap of 6.8 ± 0.2 eV, while optical spectroscopy revealed an exciton binding energy of 0.7 ± 0.2 eV. With hBN being a large-band-gap

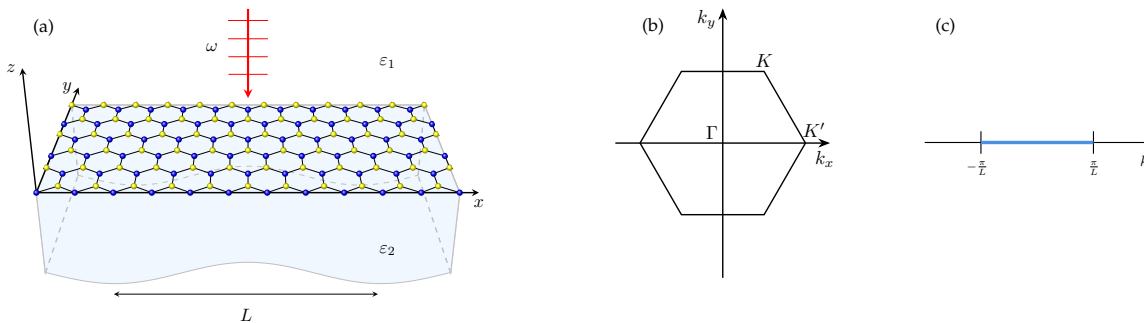


FIG. 1: (a) A hBN monolayer over a substrate, subjected to an external periodic potential with period L along the x -direction, under a time-periodic drive of a linearly polarized optical field. (b) Brillouin zone (BZ) of the original monolayer hBN, and (c) the BZ of the superlattice resulting from applying the 1D potential of (a).

insulator, excitonic effects play an important role in its optical properties in the deep UV range [33]. This was shown when an experimental measurement of photoluminescence of monolayer hBN on quartz [19] reported an optical resonance around 6.1 eV, that can only be explained by taking excitonic effects into account.

When studying the sub-gap optical properties of hBN, we cannot ignore the fact that the exciton can excite an EM mode confined at the surface of the 2D material, called exciton polariton. The intriguing properties of polaritons allow for the detection of small changes in the refractive index of the surrounding material, rendering the 2D material viable for the fabrication of optoelectronic sensors. Given the energy scales of the band gap and exciton binding energies of hBN, one can think of it as a good candidate for the detection of bio-molecules that present resonances in the UV, such as cyclic β -helical peptides, relevant for the biophysics of the human body [34].

In this work, we propose means of manipulating the optoelectronic properties of hBN by applying a one-dimensional (1D) periodic potential on a monolayer, as represented in Fig. 1(a). As we will see, the resultant superlattice has distinct electronic properties from the pristine hBN monolayer. The layer is deposited on a quartz substrate, and is illuminated from above with monochromatic light, linearly polarized along either the x or the y -axis. This driving field will allow the formation of excitons that, by coupling with light, will give rise to exciton polaritons propagating along the sample.

This paper is organized as follows: In Sec. II we derive the renormalized low-energy Hamiltonian, from which we can extract the emergent electronic structure of hBN with a 1D periodic potential on top. In Sec. III we introduce the formalism adopted for the calculation of the excitonic optical response of the system under study. In Sec. IV we provide results for the new excitonic physics, and the consequences it brings to the sub-gap optical response, namely the optical conductivity and optical absorption. We finish the section with a study of the spatial confinement of transverse magnetic (TM) exciton polaritons. In Sec. V we summarize our main results and offer our conclusions.

II. RENORMALIZED HAMILTONIAN

The electronic properties of independent electrons in 2D materials are described in terms of tight-binding models. In general, these models use a fairly large number of bands, which prevents analytical calculations of the materials' properties. Fortunately, the physics of excitons is often determined by effective models with only two bands, whose Hamiltonian can be written using Pauli matrices. These are the cases of graphene and hBN. The difference between the two systems lies in the presence of a band gap in the latter. With all this in mind, an effective, low-energy, independent-electron Hamiltonian can be written as [35]

$$H_0 = -i\hbar v_F (\sigma_x \partial_x + \sigma_y \partial_y) + M \sigma_z, \quad (1)$$

where v_F is the Fermi velocity, $E_g = 2M$ is the band gap obtained within density-functional theory (DFT) [33], and the σ 's are the Pauli matrices. The low-energy dispersion relation reads

$$E_s(\mathbf{q}) = s \frac{1}{2} \sqrt{E_g^2 + 4\hbar^2 v_F^2 (q_x^2 + q_y^2)} \approx s \left(\frac{E_g}{2} + \frac{\hbar^2 |\mathbf{q}|^2}{2m^*} \right), \quad (2)$$

where the wavevector \mathbf{q} is measured from the \mathbf{K} point in the BZ (see Fig. 1), while $m^* = E_g/2v_F^2$ is the common effective mass of electrons in the conduction band ($s = +1$) and holes in the valence band ($s = -1$), respectively. The approximation of parabolic bands is valid when the band gap is large and when looking at electronic states with small momentum (measured from the point around which we are expanding the Hamiltonian).

Since we want to describe the effect of an external potential on the electronic properties of electrons in hBN (including its excitonic properties), we introduce an external electrostatic potential $V(x)$, so that the total Hamiltonian reads

$$H = H_0 + V(x). \quad (3)$$

The potential varies only along the x -direction and has

period L , that is, $V(L+x) = V(x)$. This external potential then creates a superlattice, leading to a mini-BZ of size $[-\pi/L, \pi/L]$, as in Fig. 1(c), and the appearance of a set of mini-bands. This problem is similar to graphene under an external potential [36], but with an extra term that confers a mass to the electrons thus opening an energy gap at K of the original BZ. By introducing the external potential $V(x)$, we add an extra periodicity in the system in addition to the original lattice periodicity (already encoded in the original low-energy Hamiltonian). As noted above, we form a 1D superlattice whose reciprocal lattice vectors are given by $\mathbf{G}_\ell = \ell G_0 \hat{x}$, with $G_0 = 2\pi/L$ and ℓ an integer.

It would be convenient if we could remove the potential from the Hamiltonian (3), while maintaining the Dirac-like form of H_0 . Fortunately, this is possible via a unitary transformation written in terms of $V(x)$ and given by [36]

$$U_\alpha = \frac{1}{\sqrt{2}} \begin{pmatrix} e^{-i\alpha(x)/2} & -e^{i\alpha(x)/2} \\ e^{-i\alpha(x)/2} & e^{i\alpha(x)/2} \end{pmatrix}, \quad (4)$$

where $\alpha(x) = (2/\hbar v_F) \int_0^x dx' V(x')$. Focusing on electronic states whose wavevector $\mathbf{k} = \mathbf{q} + \ell \mathbf{G}_0/2$, with $|\mathbf{q}| \ll G_0$, we obtain an analytical expression for the renormalized low-energy Hamiltonian, that is, the initial low-energy Hamiltonian but with renormalized parameters. For that, we use the following states as the basis functions

$$\begin{pmatrix} 1 \\ 0 \end{pmatrix} e^{i(\mathbf{q} + \ell \mathbf{G}_0/2) \cdot \mathbf{r}} \quad \text{and} \quad \begin{pmatrix} 0 \\ 1 \end{pmatrix} e^{i(\mathbf{q} - \ell \mathbf{G}_0/2) \cdot \mathbf{r}}, \quad (5)$$

and expand the exponential in a Fourier series as

$$e^{i\alpha(x)} = \sum_{\ell=-\infty}^{\infty} J_\ell(\beta) e^{i\ell G_0 x}, \quad \beta \equiv \frac{V_0 L}{\pi \hbar v_F}, \quad (6)$$

where J_ℓ is the Bessel function of the first kind of order ℓ . After applying the unitary transformation, computing the matrix elements for the previous basis states, and changing to a basis made of a symmetric and anti-symmetric combination of the previous states, we obtain the renormalized low-energy Hamiltonian

$$\bar{H} = \frac{\ell}{2} G_0 \hbar v_F + \hbar v_F [\sigma_x q_x + \sigma_y J_\ell(\beta) q_y] - \sigma_z M J_\ell(\beta). \quad (7)$$

Here, the first term simply shifts the energies. Since ℓ is an integer, we have now multiple bands, whose emergence can also be predicted by the theory of nearly-free electrons. The comparison between the two treatments is done in App. A. In Eq. (7), we notice that for a quasiparticle propagation along the y -direction the group velocity is renormalized as $v_F \rightarrow J_\ell(\beta) v_F$. Since $|J_\ell(\beta)| < 1$, the slope of the dispersion along the y -direction is smaller than along the x -direction. This gives rise to an anisotropic Dirac cone. Also, the band gap $E_g = 2M$ changes as $E_g \rightarrow E_g |J_\ell(\beta)|$. Therefore, it is possible to reduce the pristine gap of hBN by choosing

an appropriate value for β . With this mechanism we can control both the gap and the excitonic states, which now become the excitons of a synthetic anisotropic material, that resembles naturally occurring anisotropic materials, such as phosphorene.

Next, we explore the consequences of the introduction of the 1D potential in the electronic properties of hBN. From the renormalized low-energy Hamiltonian (7), we infer the low-energy dispersion (up to a global shift in the energies)

$$E_s(\mathbf{q}) = s \frac{1}{2} \sqrt{E_g^2 J_\ell^2(\beta) + 4\hbar^2 v_F^2 [q_x^2 + q_y^2 J_\ell^2(\beta)]}, \quad (8)$$

which is now anisotropic, while we recover the isotropic Eq. (2) for $\beta \rightarrow 0$ and $\ell = 0$. This deformed paraboloid has two distinct effective masses $m_x = m^* |J_\ell(\beta)|$ and $m_y = m^* / |J_\ell(\beta)|$ along the x and y -directions, respectively. The eigenproblem $\bar{H}|s, \mathbf{q}\rangle = E_s(\mathbf{q})|s, \mathbf{q}\rangle$ has an analytical solution for the spinors

$$|+, \mathbf{q}\rangle = \begin{pmatrix} e^{-i\theta_q(\beta)} \sin\left(\frac{\xi_q}{2}\right) \\ \cos\left(\frac{\xi_q}{2}\right) \end{pmatrix}, \quad (9a)$$

$$|-, \mathbf{q}\rangle = \begin{pmatrix} \cos\left(\frac{\xi_q}{2}\right) \\ -e^{i\theta_q(\beta)} \sin\left(\frac{\xi_q}{2}\right) \end{pmatrix}, \quad (9b)$$

where $\xi_q = \arctan\left(\frac{2\hbar v_F q(\beta)}{J_\ell(\beta) E_g}\right)$, with $q(\beta) = \sqrt{q_x^2 + J_\ell^2(\beta) q_y^2}$, and $\theta_q(\beta) = \arctan[J_\ell(\beta) \tan \theta]$, with $\tan(\theta) = q_y/q_x$. These spinors will be useful later on to compute the optical conductivity.

III. EXCITONIC CONTRIBUTIONS TO SUB-GAP OPTICAL RESPONSE

The presence of the external potential $V(x)$ influences considerably the electronic properties of hBN, by rendering the low-energy dispersion anisotropic. This brings consequences to the excitonic physics, and subsequently to the optical response. There are several approaches to the calculation of the excitonic properties of a semiconductor or a band insulator. Excitons with a radius large enough compared to the lattice spacing are denoted Wannier excitons. The general approach to determine the exciton energy levels and wavefunctions is the solution of the Bethe-Salpeter equation [37] in momentum space. This microscopic approach is powerful but often computationally demanding. It would then be desirable to have in reach a simpler approach that still captures the essence of the exciton physics. Starting from a microscopic approach [38], if some —relatively flexible— conditions are met, the Fourier transform of the Bethe-Salpeter equation transforms into an effective Schrödinger equation with an electrostatic attractive potential called the Wannier equation. The method of the Wannier equation has

been benchmarked against the Bethe–Salpeter equation with good results, as the latter equation accounts for fine details only [38].

The Wannier equation can be solved, among others, with the variational method, which allows for a good approximation of the energies and approximate analytical expressions for the excitonic wavefunctions. This approach has previously been applied to black phosphorus [39] and TMDs [40, 41], with significant accuracy.

A. Variational method

The variational method [42] consists in using a trial wavefunction, that depends on a set of parameters, to compute the expectation value of the Hamiltonian H and minimize it with respect to said parameters. Symbolically, we define a state $|\psi_\alpha(\mathbf{r})\rangle$, with α representing the set of unknown parameters. Then we compute $E_\alpha = \langle \psi_\alpha(\mathbf{r}) | H | \psi_\alpha(\mathbf{r}) \rangle$ and solve $\partial E / \partial \alpha = 0$ for α . Finally, we return to E_α and substitute the optimal values for α .

The Hamiltonian H pertains to the system comprised of an electron–hole pair,

$$H = \frac{p_x^2}{2\mu_x} + \frac{p_y^2}{2\mu_y} + V_{\text{RK}}(r), \quad (10)$$

where the first two terms correspond to the kinetic contribution, with μ_x and μ_y being the electron–hole reduced masses along the x and y -directions, respectively, and the last term corresponding to the electrostatic attraction between the electron and the hole in the 2D material, here given by the electrostatic Rytova–Keldysh (RK) potential [37]

$$V_{\text{RK}}(r) = -\frac{e^2}{4\pi\epsilon_0 r_0} \frac{\pi}{2} \left[\mathbf{H}_0 \left(\frac{\kappa r}{r_0} \right) - Y_0 \left(\frac{\kappa r}{r_0} \right) \right]. \quad (11)$$

Here, r_0 is a screening length parameter, κ is the average between the relative permittivity of the substrate ϵ_2 and the cladding material surrounding the 2D material ϵ_1 , and ϵ_0 is the vacuum permittivity. Finally, \mathbf{H}_0 is the Struve function of order zero and Y_0 is the Bessel function of the second kind of order zero. The exciton dynamics is determined by the Wannier equation $E_b \psi = H \psi$, which is a Schrödinger-like equation, where H is the Hamiltonian given in Eq. (10), ψ is the exciton wavefunction and $E_b = E - \Delta$ is the exciton binding energy, while E is the energy level of the exciton and Δ the band gap. To obtain the energy levels of the exciton we have to compute the binding energies and the band gap. For the former, we apply the variational method to the first four excitonic states $1s$, $2x$, $2y$ and $2s$, and use trial wavefunctions that resemble the solutions of the 2D hydrogen atom, but taking into account the effect of the anisotropy in the mass tensor. The form of each wavefunction is given in App. C 1, and the details of the calculations for

finding the variational parameters are given in [39]. The band gap is the sum of the renormalized DFT gap and the electron–electron exchange correction, both contributions renormalizing with the potential (see App. B for details).

B. Optical conductivity

Subjecting the excitonic material to an external and monochromatic EM field with frequency ω , the optical conductivity, within the linear response and in the dipole approximation, is given by [43]

$$\sigma(\omega) = \frac{e^2}{8\pi^3 i \hbar} \sum_\nu \left[\frac{E_\nu |\Omega_\nu|^2}{E_\nu - (\hbar\omega + i\Gamma)} + \frac{E_\nu |\Omega_\nu|^2}{E_\nu + \hbar\omega + i\Gamma} \right] \quad (12)$$

where E_ν is the energy of the excitonic state ν . The broadening parameter $\Gamma \ll \omega$ is the sum of the non-radiative decay due to phonons, the non-radiative decay due to impurities and the radiative decay, but its calculation is outside the scope of this work. Therefore, we made an estimation based on previous works [44]. Furthermore, Ω_ν is the Berry curvature of the excitonic state ν , being computed by $\Omega_\nu = \sum_{\mathbf{q}} \Psi_\nu(\mathbf{q}) \langle -, \mathbf{q} | \mathbf{r} \cdot \hat{\mathbf{e}} | +, \mathbf{q} \rangle$, where $\Psi_\nu(\mathbf{k})$ is the wavefunction of the excitonic state ν in momentum space, and the bracket is the optical matrix element of the dipole operator between the spinors given in Eq. (9). The unit vector $\hat{\mathbf{e}}$ is dictated by the polarization of the wave, and herein we consider light polarized along either the x and the y -directions. As the system is anisotropic, the conductivity will be different depending on the polarization of the incident EM field. As explained in App. C, we have two distinct conductivities σ_{xx} and σ_{yy} for light polarized along the x and y -directions, respectively. Knowing the optical conductivity, we compute the sub-gap optical absorption through

$$\mathcal{A} = 1 - \mathcal{R} - \text{Re} \left\{ \sqrt{\frac{\epsilon_2}{\epsilon_1}} \right\} \mathcal{T}, \quad (13)$$

where the reflection and transmission coefficients \mathcal{R} and \mathcal{T} follow from Fresnel’s equations for normal incidence on a conductive material cladded between two dielectrics [45]. We note that the relative permittivities that enter in Eq. (13) are the dynamic dielectric functions of the respective materials. In the electron–electron or electron–hole interaction, the relevant quantities are the static permittivities of the materials. In the end, the dependence is only on the average between the static permittivities, that we denoted by κ in Eq. (11).

IV. RESULTS AND DISCUSSION

We have seen that the 1D external potential influences the electronic properties of hBN. In particular, it renormalizes the gap and the effective masses, depending on

the strength and period of the potential. In fact, by inspection of the renormalized low-energy Hamiltonian in Eq. (7), we can claim that the renormalized parameters depend only on the product V_0L between the strength and period of the potential. Hence, for a complete analysis, it only suffices to study the system varying β . The surrounding medium is air ($\varepsilon_1 = 1$), while for the substrate we choose silicon dioxide (SiO_2). The static dielectric function of SiO_2 is $\varepsilon_2(\omega \rightarrow 0) = 3.9$, and in the UV range it is essentially constant, with $\varepsilon_2(\omega) \approx 2.16$.

A. Excitonic binding energies

As we have seen in Sec. II, the effective masses renormalize as $m_x = m^*/|J_0(\beta)|$ and $m_y = m^*/|J_0(\beta)|$. This means that as $J_0(\beta) \rightarrow 0$, the dispersion becomes more and more anisotropic. To study the effects of this anisotropy in the electronic properties of the system at hand, we compute the band gap and the binding energies of the excitonic states $1s$, $2x$, $2y$ and $2s$ for varying β , from the case $\beta = 0$ without potential, to $\beta = 2.3$ sufficiently close to the zero of the Bessel function $J_0(\beta)$. We stress that the band gap includes the electron–electron exchange correction, that also renormalizes with β (see App. B). The results are displayed in Fig. 2. It can be seen in Fig. 2(a) that by manipulating the value of β , we can tune the band gap. When β reaches the zero of $J_0(\beta)$, the gap closes. Regarding the binding energies, Fig. 2(b) shows that the anisotropy lifts the degeneracy between the states $2x$ and $2y$. Also, the binding energies of the states $1s$, $2x$ and $2s$ decrease as we increase β , but that of the $2y$ state is non-monotonic. Nonetheless, the state $2y$ is always the first excited state. Initially, the second excited state is $2x$, but for $\beta \approx 1.5$, the $2s$ takes its place.

B. Optical conductivity and Absorption

A recent experimental work [19] showed that single-layer hBN displays optical activity in the UV range. The measured photoluminescence exhibits two sharp peaks at a frequency around 6.1 eV. These peaks are excitonic in nature, and their theoretical prediction in [44] agrees very well with the experimental measurement. Here we apply the same theory as in [44] to compute the optical absorption of monolayer hBN subjected to the external periodic potential. But first, we computed the optical conductivity using Eq. (12) for selected values of β , to obtain the results displayed in Figs. 3a-3d. Since the optical conductivity is complex, we plot separately the real part in Figs. 3a and 3c, and the imaginary part in Figs. 3b and 3d. In the calculation we focus on the excitonic states $1s$ and $2s$, while the states $2x$ and $2y$ do not contribute to the conductivity. We also considered both cases of light polarized along the x and y axes. We observe a tendency of a redshift in the peaks as we increase β , and

consequently the anisotropy of the system. We note that the energy level E_ν of the excitonic state ν is given by $E_\nu = E_{b,\nu} + \Delta$, where $E_{b,\nu}$ is the respective binding energy and Δ the band gap, quantities computed in the previous section. For light polarized along the x -axis, we observe in Figs. 3a and 3c that the peaks of the conductivity coming from the $1s$ and $2s$ states are enhanced as we increase β . On the other hand, the peaks in the conductivity for light polarized along the y -direction are attenuated.

One can notice also in Fig. 3b that for the case $\beta = 2.3$, the excitonic states $1s$ and $2s$ become so close, that the imaginary part of the conductivity $\text{Im}\{\sigma(\omega)\}$ has only one zero. We expect that this influences the character of the polaritons, since the sign of $\text{Im}\{\sigma(\omega)\}$ dictates which kind of polaritons, transverse magnetic (TM) or transverse electric (TE) the 2D material supports, as we will explain in Sec. IV C.

We can now compute the optical absorption at normal incidence using Eq. (13). Figs. 4a and 4b display the optical absorption for the same values of β as in Fig. 3, for light polarized along the x and y -directions, respectively. Interestingly, the behaviour of the absorption is not as simple as that of the conductivity. For instance, let us look at Fig. 4a. The peak due to the $1s$ state seems to attenuate from right to left, as we increase β . In contrast, the peak due to the $2s$ state seems to intensify. To study this behaviour more carefully, in Fig. 4c we plot the value of the absorption peaks due to the $1s$ (black lines) and $2s$ (red lines) states separately, for polarization along the x (continuous lines) and y directions (dashed lines), as a function of β , which is allowed to vary continuously. Indeed, we see that for polarization along the x axis the $1s$ peak decreases monotonically as we approach the zero of $J_0(\beta)$, while the $2s$ peak tends to increase, until it reaches a maximum right before the zero of the Bessel function. Interestingly, we can have a $2s$ peak more intense than a $1s$ peak, a feature that can be observed in Figs. 4a (notice the green and red curves) and 4c. This phenomenon has already been observed experimentally [46] and explained theoretically [47]. For light polarized along the y -direction, one can observe that the absorption for light polarized along the y -direction is not as intense as for light polarized along the x -direction. Furthermore, from Fig. 4c, we can note that it is now the $2s$ peak that decreases monotonically, while the $1s$ peak is maximum for $\beta \approx 0.9$.

C. Exciton polaritons

Polaritons are light–matter hybrids, arising from the strong-coupling of elementary excitations of a 2D material with light. Polaritonic modes are characterized by an evanescent decay away from the material and a strong enhancement of the EM field in its vicinity. There are many kinds of polaritons, like phonon polaritons, plasmon polaritons, magnon polaritons and exciton polaritons [48].

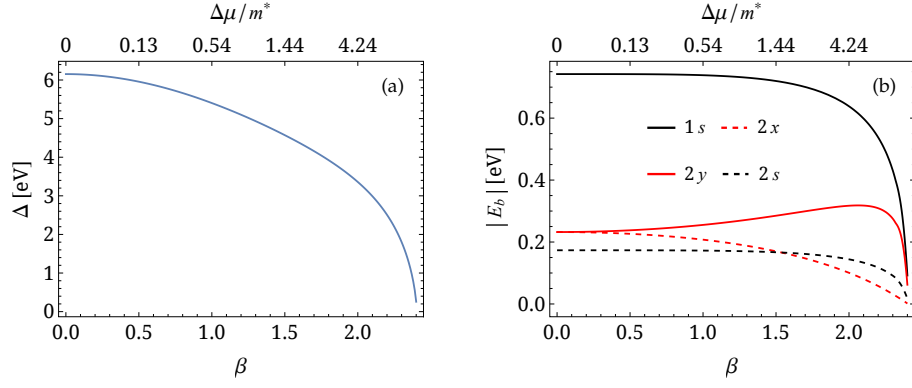


FIG. 2: (a) Band gap and (b) binding energies of the excitonic states $1s$ (black continuous line), $2x$ (red dashed line), $2y$ (red continuous line) and $2s$ (black dashed line) as a function of β . In both panels, the top horizontal axis displays the value of the effective mass anisotropy defined as $\Delta\mu = (m_y - m_x)/m^*$. For hBN, the parameters are [33]: $E_g = 3.92$ eV, $\hbar v_F = 5.06$ eV·Å, and $r_0 = 10$ Å. For the surrounding medium we have air with $\varepsilon_1 = 1$, while for the quartz substrate $\varepsilon_2 = 3.9$.

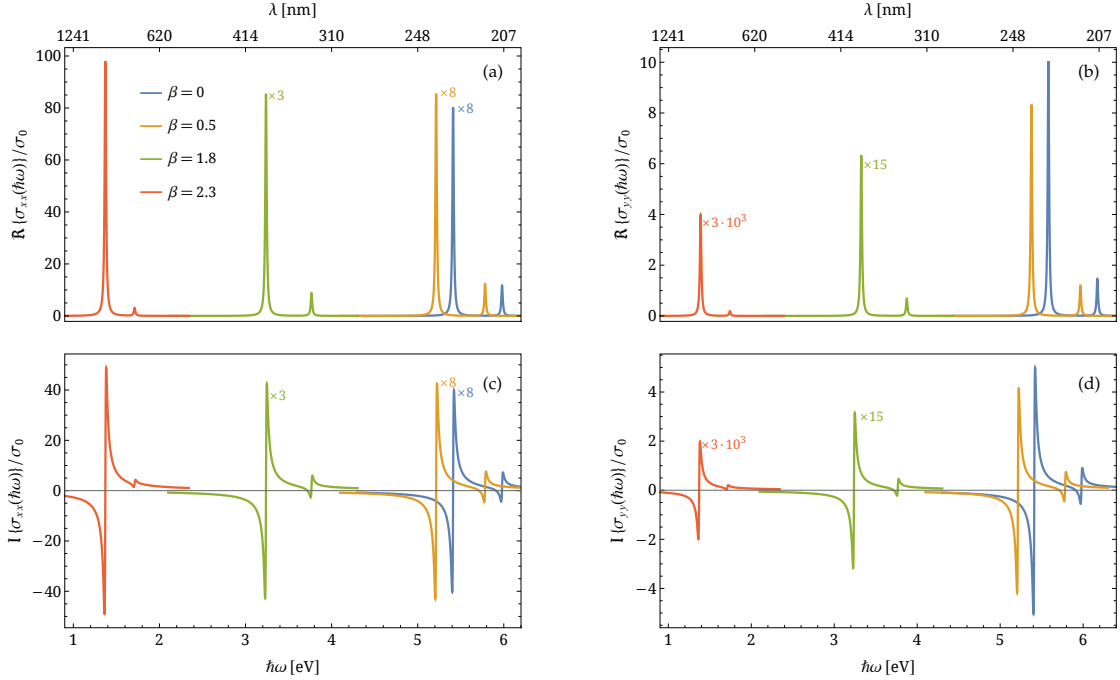


FIG. 3: Sub-gap optical conductivity of hBN under a 1D periodic potential, as depicted in Fig. 1. Panels (a) and (b) show the real and imaginary parts of the conductivity, respectively, for light polarized along the x -axis. Panels (c) and (d) show the real and imaginary parts of the conductivity, respectively, for light polarized along the y -axis. The inset in panels (a) and (b) show a zoom-in of the real and imaginary parts of the conductivity, respectively, for the cases $\beta = 0$ and $\beta = 0.53$. Results for different β have been rescaled as noted in each panel, for clarity. We used $\Gamma = 10$ meV, and for the quartz substrate $\varepsilon_2 = 2.16$.

Here we are concerned only with exciton polaritons. The dispersion relation of the polariton depends on the polarization of the EM field. For TE modes, the electric field is in the plane of the 2D material, and perpendicular to the wavevector of the polariton, while the magnetic field lies on the xz -plane. The dispersion relation for TE modes is

$$\kappa_1 + \kappa_2 - i\omega\mu_0\sigma_{yy}(\omega) = 0, \quad (14)$$

where ε_j , $j = 1, 2$, is the relative electric permittivity of the two media cladding the hBN layer in the frequency region herein considered, $\kappa_j = \sqrt{q^2 - \varepsilon_j\omega^2/c^2}$, ω is the frequency of the polariton, q is the in-plane wavenumber, and μ_0 is the vacuum magnetic permeability.

For TM modes, it is the magnetic field that lies on the plane of the 2D material, while the electric field is in the

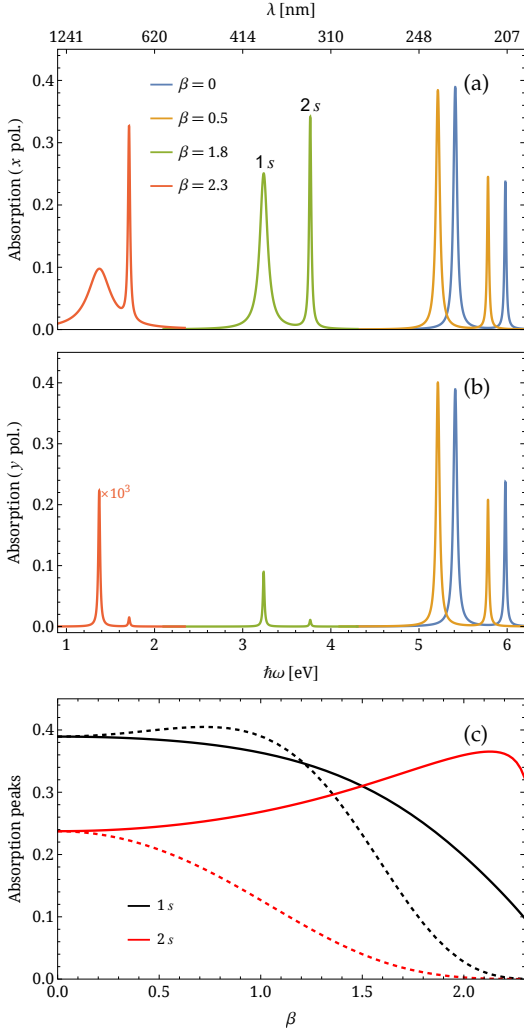


FIG. 4: Sub-gap optical absorption of hBN under a 1D periodic potential. Panels (a) and (b) show the absorption for light polarized along the x and y -directions, respectively. Each color corresponds to a different value of β , where $\beta = 0$ corresponds to the case with no potential. We used the same values for β of Fig. 3. For each realization, two peaks are observed. The one occurring at lower energy corresponds to the $1s$ state, while the other corresponds to the $2s$ state. Panel (c) shows the values of the absorption peaks due to the excitonic states $1s$ (black lines) and $2s$ (red lines) as a function of β for light polarized along the x (continuous lines) and y (dashed lines) directions, respectively. Note that for each value of β the peaks occur at different energies, as one can see in panels (a) and (b).

xz -plane. Their dispersion relation is

$$\frac{\varepsilon_1}{\kappa_1} + \frac{\varepsilon_2}{\kappa_2} + i \frac{\sigma_{xx}(\omega)}{\varepsilon_0 \omega} = 0. \quad (15)$$

As a rule of thumb, TE modes are supported when the imaginary part of the conductivity is negative, whereas TM modes are supported when the imaginary part of

the conductivity is positive. The solutions of the previous two equations, that can only be obtained numerically, gives the dispersion relation $\omega(q)$, where the wavenumber has now an imaginary part, since the conductivity is complex. It is important to highlight that in Eqs. (14) and (15) two different conductivities appear. In isotropic systems, such as the case of monolayer hBN, the conductivities σ_{xx} and σ_{yy} coincide. However, they are in general different, as we have seen in the previous section.

Regarding the TE modes, we observe that they are either very poorly confined and present a similar dispersion to free light as expected [45, 49], or they do not exist at all [that is, Eq. (14) does not present any solution]. Hence, we omit the analysis for TE modes, as they are not relevant. We focus then on TM modes solely. To obtain the dispersion relation $\omega(q)$ for TM polarized polaritons, we solve numerically Eq. (15) in the regions where $\text{Im}\{\sigma(\omega)\} > 0$, for different values of β . In general, the imaginary part of the conductivity admits more than one zero, and in our case, we have observed in Sec. IV B that it has either two or one. The main region of frequencies of interest is that between the first and second zeros, in the case $\text{Im}\{\sigma(\omega)\}$ does have two zeros. After the third zero, we are very near the bottom of the conduction band, where the sub-gap conductivity we computed herein is not accurate. To compute the conductivity above the gap, one needs to also consider unbound states [50].

The dispersion relation of TM modes is presented in Figs. 5a-c, for three different values of β . The case $\beta = 0$ (Fig. 5a) represents hBN with no potential on top, and we also choose an intermediate case $\beta = 0.5$ (Fig. 5b), and an extreme case $\beta = 2.3$ (Fig. 5c). The case without potential and the intermediate case share similar features, namely the dispersive behaviour very distinct from free light, with the real part of the wavenumber $\text{Re}\{q\}$ reaching a high maximum value at a specific frequency, and the high degree of confinement given the high values that $\text{Im}\{q\}$ can reach. However, the $\beta = 2.3$ case of Fig. 5c is qualitatively different. This is due to the facts that in this case the imaginary part of the conductivity has only one zero and the conductivity peaks at higher values. As a consequence, the dispersion behaves like free light in SiO_2 for low frequencies and then behaves like the previous two cases, with $\text{Re}\{q\}$ achieving a maximum around $36 \mu\text{m}^{-1}$. Then, the dispersion bends until $\text{Re}\{q\}$ reaches a minimum of $14 \mu\text{m}^{-1}$, and afterwards it increases back again [51]. The degree of confinement is also lower in this case, as can be seen by the different wavenumber scales (nm^{-1} in Figs. 5a and 5b, μm^{-1} in Fig. 5c). To gain intuition on the confinement of the polariton, we show in Fig. 7 a spatial map of the EM field of a TM mode in the vicinity of the interface between air and the substrate.

V. CONCLUSION AND OUTLOOK

With the advent of the experimental realization of 2D materials, the way of manipulating the electronic prop-

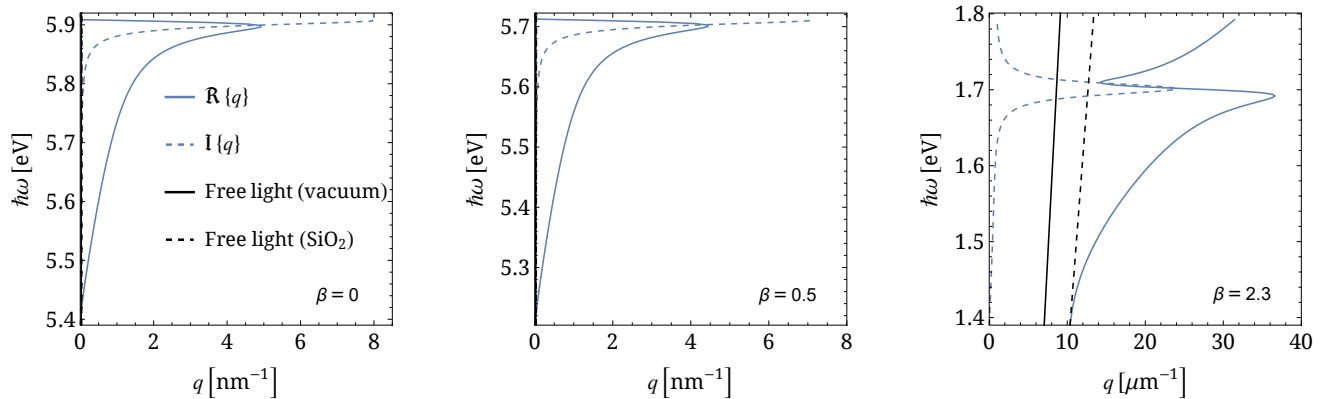


FIG. 5: The dispersion relation $\omega(q)$ for exciton polaritons. We solve numerically Eq. (15) for different values of β . The solution is the frequency as a function of the wavenumber, that has a real part (solid blue line) and an imaginary part (dashed blue line). For comparison, we show the dispersion relation for free propagating light in vacuum (solid black line) and in SiO_2 (dashed black line). The case $\beta = 0$ represents monolayer hBN without potential on top.

erties of 2D materials by applying an additional periodic modulation has gained significant attention. Notwithstanding the current popularity of this topic, the idea of forming superlattices to manipulate the properties of materials dates back to the end of the last century, with studies on plasmonic excitations in externally modulated 2D electron-gases [52, 53]. The periodic modulation can result from combining two monolayers to form a bilayer structure and applying a twist to form a moiré superlattice [54, 55], or even by combining bulk systems, like for example two hBN slabs, bringing their surfaces together and applying a twist [56].

In our case, the external potential can be imposed by a periodic patterned back/top gate. The tuning of the potential has a high degree of flexibility, since our predictions depend only on the product of the strength of the potential with its period, but not on both independently. In a typical semiconductor, the exciton size is of the order of 5 nm. For the period, we need to choose a high enough value compared to the exciton radius, so of the order of 40 nm. For this length scale and to have $\beta \sim 1$, we need a potential amplitude of the order of 40 meV, which is feasible in experiments. However, our theory does not make predictions when β matches exactly the zero of the Bessel function, since the renormalized effective mass along x vanishes and that along y diverges, rendering the Wannier equation description inapplicable. Also, the simplicity of the potential allowed for an analytical expression for the renormalized low-energy Hamiltonian, but it comes with the disadvantage that a cosine potential is more difficult to implement experimentally. We remark that our theory also applies to a square periodic potential, more common in experiments. Hence, our results widely apply to a variety of periodic potential.

Our work presents a way of changing the frequency of the excitonic resonances of hBN, as an alternative to the usual one of changing the substrate. The redshift in the resonances as we increase the strength (or period) of the

potential makes it possible to make hBN optically non-trivial in between the near- and the deep-UV. Furthermore, the system response is different depending on the polarization of the incident field, which is the essential characteristic of a grid wire polarizer.

The study of excitonic and optical properties in twisted bilayer systems is a natural extension of this work. A key feature in these systems is the emergence of flat electronic bands, enhancing interactions and promoting many-body correlated states, which offer a plethora of exotic phenomena in physics [13, 15]. There are already studies of excitons in these systems [57, 58] that predict that the optical spectrum of the bilayer system is very different from that of the isolated monolayer. Furthermore, plasmon polaritons have been studied in twisted bilayer graphene as well [59], where the appearance of electronic flat bands leads to plasmon polaritons with almost constant dispersion. However, polaritonics in the UV range within the realm of twisted bilayer systems remains largely unexplored. With the experimental and technological tools available nowadays, one can expect solid developments in the field of 2D moiré structures in general, and in particular in the study of excitons [60, 61].

ACKNOWLEDGEMENTS

N. A. M. is a VILLUM Investigator supported by VILLUM FONDEN (Grant No. 16498). The Center for Polariton-driven Light–Matter Interactions (POLIMA) is funded by the Danish National Research Foundation (Project No. DNRF165). N. M. R. P. acknowledges support by the Portuguese Foundation for Science and Technology (FCT) in the framework of the Strategic Funding UIDB/04650/2020, COMPETE 2020, PORTUGAL 2020, FEDER, and through projects PTDC/FIS-MAC/2045/2021 and EXPL/FIS-MAC/0953/2021. N. M. R. P. also acknowledges the

Independent Research Fund Denmark (grant no. 2032-00045B) and the Danish National Research Foundation (Project No. DNRF165)

Appendix A: Nearly-free electron theory

As an independent check of the previous results, we now set up a quasi-free electron calculation, where the electrons described by H_0 feel the effect of the external potential $V(x)$ as a perturbation. The description of the effect of an external potential on free electrons is a well known problem in condensed-matter physics [62]. Here we apply the same reasoning to electrons in hBN. Both the wave functions and the energy bands can be obtained from [63]

$$[E - E_s(\mathbf{q})] c(s, \mathbf{q}) = \sum_{s', \mathbf{G}} U_{\mathbf{G}} \langle s, \mathbf{q} | s', \mathbf{q} - \mathbf{G} \rangle c(s', \mathbf{q} - \mathbf{G}), \quad (\text{A1})$$

where $E_s(\mathbf{q})$ is the unperturbed dispersion relation (2), while the bracket uses the spinors of the unperturbed low-energy Hamiltonian, and $U_{\mathbf{G}}$ are the Fourier components of the potential. In our case, $U_{\mathbf{G}} = V_0/2$ for $\mathbf{G} = \pm G_0 \hat{x}$, and $U_{\mathbf{G}} = 0$ otherwise. The constants $c(s, \mathbf{q})$ are the amplitudes of superposition of unperturbed electronic states allowing to retrieve the electronic wave function. In principle, Eq. (A1) is exact. However, often the summation on the right-hand side is truncated for including a finite

number of reciprocal lattice vectors. Here, we include only three reciprocal lattice vectors $G = 0, \pm 2\pi/L$. This has two consequences: (i) only the two lowest energy bands (the top valence band and the bottom conduction bands) are well described and (ii) the value of β should be smaller than 1. In Fig. 6 we compare the results from the exact approach described in the previous section and quasi-free-electron description introduced here. The agreement is good.

These results show that, at least for $\beta < 1$, we can very well approach this problem from a nearly-free-electron perspective, and the unitary transformation is not needed. One of the advantages of using this approach is that we work directly with the eigenfunctions of H_0 . However, we observed that this method breaks down if one chooses a combination of V_0 and L such that β assumes values comparable or higher than 1. We stress that the purpose of this section was to conciliate the exact result from Sec. II and the nearly-free electron theory, and in what conditions the predictions of the two different methods agree. From here onward, we work solely with the exact result.

Appendix B: Electron-electron exchange correction

The Bethe–Salpeter equation is an eigenproblem for the wavefunction $\phi_\nu(\mathbf{k})$ of the exciton in momentum space and its energy E_ν , and it writes [44]

$$E_\nu \phi_\nu(\mathbf{k}) = \phi_\nu(\mathbf{k})(E_{\mathbf{k},+} - E_{\mathbf{k},-}) - \frac{1}{A} \sum_{\mathbf{p}} \phi_\nu(\mathbf{p}) V_{\mathbf{k}-\mathbf{p}} F_{+---}(\mathbf{k}, \mathbf{p}, \mathbf{k} - \mathbf{p}) + \frac{1}{A} \phi_\nu(\mathbf{k}) \sum_{\mathbf{p}} V_{\mathbf{p}} [F_{----}(\mathbf{p} + \mathbf{k}, \mathbf{k}, \mathbf{p}) - F_{-+++}(\mathbf{p} + \mathbf{k}, \mathbf{k}, \mathbf{p})], \quad (\text{B1})$$

where the form factor

$$F_{\lambda_1 \lambda_2 \lambda_3 \lambda_4}(\mathbf{p}, \mathbf{k}, \mathbf{q}) = \langle \lambda_2, \mathbf{p} - \mathbf{q} | \lambda_3, \mathbf{p} \rangle \langle \lambda_1, \mathbf{k} + \mathbf{q} | \lambda_4, \mathbf{k} \rangle \quad (\text{B2})$$

is defined in terms of products of the spinors (9). Now we elucidate the physical meaning of the different terms in Eq. (B1). The first term on the right-hand side accounts for the gain in energy by exciting an electron in the valence band to the conduction band, without accounting for electron–hole interactions. The second term accounts for the interaction between the electron in the conduction band and the hole in the valence band. The third term corresponds to the electron–electron exchange corrections to the bands, and it is the one in which we are interested now. To compute the exchange correction to the band gap, we compute the sum over momentum in the third term of the Bethe–Salpeter equation (B1) for $\mathbf{k} = 0$. Denoting the exchange correction to the gap by

Δ_{ex} , we have

$$\Delta_{\text{ex}} = \frac{1}{A} \sum_{\mathbf{p}} V_{\mathbf{p}} [F_{----}(\mathbf{p}, 0, \mathbf{p}) - F_{-+++}(\mathbf{p}, 0, \mathbf{p})]. \quad (\text{B3})$$

The form factors evaluate to $F_{----}(\mathbf{p}, 0, \mathbf{p}) = |\langle -, 0 | -, \mathbf{p} \rangle|^2 = \cos^2(\xi_p/2)$ and $F_{-+++}(\mathbf{p}, 0, \mathbf{p}) = |\langle +, 0 | -, \mathbf{p} \rangle|^2 = \sin^2(\xi_p/2)$, so that

$$\Delta_{\text{ex}} = \frac{1}{A} \sum_{\mathbf{p}} V_{\mathbf{p}} \cos(\xi_p) = \frac{1}{A} \sum_{\mathbf{p}} V_{\mathbf{p}} \frac{1}{\sqrt{1 + \left(\frac{2\hbar v_F p(\beta)}{J_0(\beta) E_g} \right)^2}}. \quad (\text{B4})$$

To proceed, we need to convert the sum into an integral, and the expression for $V_{\mathbf{p}}$, which is simply the Fourier transform of the Rytova–Keldysh potential. It

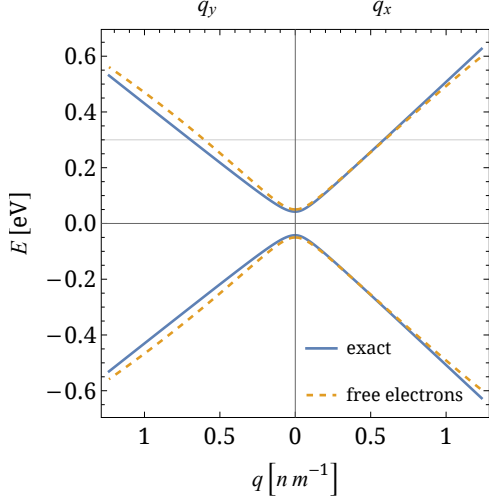


FIG. 6: Renormalized original low-energy dispersion, obtained from the exact Hamiltonian Eq. (7), and from solving numerically Eq. (A1), in blue and dashed yellow lines, respectively. The particular example with $M = 50$ meV is for $\beta = 0.8$. The right side of the plot represents the dispersion as a function of q_x for $q_y = 0$, while the left one is for dependence on q_y with $q_x = 0$. The horizontal line is a to guide the eye, so that it is easier to notice that the dispersion is anisotropic. For this plot we chose the actual value for $\hbar v_F$ for hBN, but a smaller value for the gap, for illustration reasons.

reads

$$V_{\mathbf{p}} = \frac{e^2}{2\varepsilon_0 p(r_0 p + \kappa)}, \quad (\text{B5})$$

and turning the sum into an integral and introducing the auxiliary function $\gamma(\theta) = \sqrt{\cos^2(\theta) + J_0^2(\beta) \sin^2(\theta)}$ we get

$$\Delta_{\text{ex}} = \frac{e^2}{8\pi^2 \varepsilon_0 \kappa} \int_0^{2\pi} \int_0^\infty \frac{dp d\theta}{\left(1 + \frac{r_0 p}{\kappa}\right) \sqrt{1 + \left(\frac{2\hbar v_F p \gamma(\theta)}{k_0}\right)^2}}, \quad (\text{B6})$$

where $k_0 = |J_0(\beta)| E_g / 2\hbar v_F$ is the characteristic wavenumber that depends on β . The radial integral can be performed analytically by making the change of variables $\tan(u) = p\gamma(\theta)/k_0$, leading to the expression

$$\Delta_{\text{ex}} = \frac{e^2}{8\pi^2 \varepsilon_0} \frac{k_0^2 r_0}{\kappa^2} \int_0^{2\pi} d\theta \frac{\ln \left[\frac{1 + \alpha(\theta) + \sqrt{1 + \alpha^2(\theta)}}{1 + \alpha(\theta) - \sqrt{1 + \alpha^2(\theta)}} \right]}{\alpha(\theta) \sqrt{1 + \alpha^2(\theta)}} \quad (\text{B7})$$

with $\alpha(\theta) \equiv r_0 k_0 \gamma(\theta) / \kappa$. We are not aware of any analytical solution, but the angular integral can be evaluated numerically.

Appendix C: Calculation of the Optical conductivity

We give details on the calculation of the Berry curvature

$$\Omega_\nu = \sum_{\mathbf{q}} \Psi_\nu(\mathbf{q}) \langle -, \mathbf{q} | \mathbf{r} \cdot \hat{\mathbf{e}} | +, \mathbf{q} \rangle. \quad (\text{C1})$$

The main elements that we need are the wavefunction of the excitonic state in momentum space, and the optical matrix element, which is the same for all states.

1. Fourier transform of excitonic wavefunctions

For the variational method, we used the following trial wavefunctions:

$$\Psi_{1s}(x, y) = C_{1s} e^{-\sqrt{a_{1s} x^2 + b_{1s} y^2}}, \quad (\text{C2a})$$

$$\Psi_{2x}(x, y) = C_{2x} x e^{-\sqrt{a_{2x} x^2 + b_{2x} y^2}}, \quad (\text{C2b})$$

$$\Psi_{2y}(x, y) = C_{2y} y e^{-\sqrt{a_{2y} x^2 + b_{2y} y^2}}, \quad (\text{C2c})$$

$$\Psi_{2s}(x, y) = C_{2s} \left(1 - d \sqrt{a_{2s} x^2 + b_{2s} y^2}\right) e^{-\sqrt{a_{2s} x^2 + b_{2s} y^2}}. \quad (\text{C2d})$$

For each one of the states $1s$, $2x$, $2y$, and $2s$, we have two variational parameters denoted by a and b , which account for the anisotropy of the Hamiltonian. In the isotropic case, $a = b$ for each state and then the variational wavefunctions coincide with those of the 2D hydrogen atom. We stress that the major difference between 2D Hydrogen and pristine hBN is the form of the electrostatic potential. The prefactors denoted by C are normalization constants, and all states must be orthogonal to each other. By symmetry, the s states and the p states are orthogonal, and the states p are also orthogonal to each other. Orthogonality between the $1s$ and $2s$ states can be achieved by imposing $\int d\mathbf{r} \Psi_{2s}^* \Psi_{1s} = 0$, obtaining in this way an expression for d , that depends on a_{2s} and b_{2s} , which in turn depend on the previously calculated a_{1s} and b_{1s} . The details of how the variational parameters for each state are calculated can be consulted in [39].

The momentum-resolved wavefunction of the state ν is obtained by Fourier transforming the respective wavefunction defined in real space. For the ground state $1s$ the 2D Fourier transform $\Psi(\mathbf{k}) = \int d\mathbf{r} e^{-i\mathbf{k}\cdot\mathbf{r}} \Psi(\mathbf{r})$ gives

$$\Psi_{1s}(\mathbf{k}) = \frac{2\sqrt{2\pi}}{(a_{1s} b_{1s})^{1/4}} \left(1 + \frac{k_x^2}{a_{1s}} + \frac{k_y^2}{b_{1s}}\right)^{-3/2}, \quad (\text{C3a})$$

where we performed the change of variables $x =$

$\rho/\sqrt{a_{1s}} \cos(\theta)$, $y = \rho/\sqrt{b_{1s}} \sin(\theta)$, and computed the radial and angular integrals analytically. We note that even though the expression is analytical, it has a non-trivial angular dependence. The excited states considered in this work have also analytical expressions for the Fourier transforms

$$\Psi_{2x}(\mathbf{k}) = -C_{2x} \frac{3i\pi k_x/a_{2x}}{\left(1 + \frac{k_x^2}{a_{2x}} + \frac{k_y^2}{b_{2x}}\right)^{5/2}}, \quad (\text{C3b})$$

$$\Psi_{2y}(\mathbf{k}) = -C_{2y} \frac{3i\pi k_y/b_{2y}}{\left(1 + \frac{k_x^2}{a_{2y}} + \frac{k_y^2}{b_{2y}}\right)^{5/2}}, \quad (\text{C3c})$$

$$\Psi_{2s}(\mathbf{k}) = C_{2s} 2\pi \frac{1 - 2d + (1 + d) \left(\frac{k_x^2}{a_{2s}} + \frac{k_y^2}{b_{2s}}\right)}{\left(1 + \frac{k_x^2}{a_{2s}} + \frac{k_y^2}{b_{2s}}\right)^{5/2}}, \quad (\text{C3d})$$

where calculation details are similar to the case of the state $1s$.

2. Optical matrix element

The optical matrix element can be obtained by using the relation

$$\langle -, \mathbf{q} | \mathbf{r} | +, \mathbf{q} \rangle = \frac{\langle -, \mathbf{q} | [H, \mathbf{r}] | +, \mathbf{q} \rangle}{E_{-, \mathbf{q}} - E_{+, \mathbf{q}}}, \quad (\text{C4})$$

and the canonical commutation relations to evaluate the commutator, to yield

$$\begin{aligned} \langle -, \mathbf{q} | \mathbf{r} | +, \mathbf{q} \rangle &= \frac{i\hbar v_F}{E_{-, \mathbf{q}} - E_{+, \mathbf{q}}} \left[\cos^2\left(\frac{\xi_q}{2}\right) [\hat{x} - iJ_\ell(\beta)\hat{y}] \right. \\ &\quad \left. - e^{-2i\theta_q(\beta)} \sin^2\left(\frac{\xi_q}{2}\right) [\hat{x} + iJ_\ell(\beta)\hat{y}] \right]. \end{aligned} \quad (\text{C5})$$

In the isotropic case, the previous expression dictates

that only the s and d states contribute to the optical conductivity. The term with cosine contributes only for s states, while the term with sine contributes only for d states. However, in our case, the imaginary exponential has a non-trivial dependence on the angle θ . Explicitly, $\exp[-2i\theta_k(\beta)] = \exp\{-2i \arctan[J_\ell(\beta) \arctan(\theta)]\}$. In this way, the term with the sine gives a contribution to the Berry curvature for s states in the anisotropic case. So we write the Berry curvature $\Omega_\nu = \Omega_\nu^{\cos} + \Omega_\nu^{\sin}$ as a sum of two contributions. We also note that in the optical matrix element, the terms along y -direction have an extra factor of $J_\ell(\beta)$, resulting in different conductivities depending on the polarization of the incident field.

To compute the Berry curvature (C1), we convert the sum over momentum into an integral, for which the following auxiliary function will be useful

$$\sigma(\theta) = \sqrt{\frac{\cos^2(\theta)}{a_{1s}} + \frac{\sin^2(\theta)}{b_{1s}}}. \quad (\text{C6})$$

With these functions, we can write the quantities

$$\begin{aligned} E_{-, \mathbf{q}} - E_{+, \mathbf{q}} &= \sqrt{E_g^2 J_\ell^2(\beta) + 4\hbar^2 v_F^2 q^2 \gamma^2(\theta)}, \\ \cos^2\left(\frac{\xi_q}{2}\right) &= \frac{1}{2} + \frac{1}{2\sqrt{1 + \left(\frac{2\hbar v_F q \gamma(\theta)}{J_\ell(\beta) E_g}\right)^2}}, \\ \sin^2\left(\frac{\xi_q}{2}\right) &= \frac{1}{2} - \frac{1}{2\sqrt{1 + \left(\frac{2\hbar v_F q \gamma(\theta)}{J_\ell(\beta) E_g}\right)^2}}, \end{aligned} \quad (\text{C7})$$

that appear in the optical matrix element, and for the ground state wavefunction

$$\Psi_{1s}(\mathbf{k}) = \frac{2\sqrt{2\pi}}{(a_{1s} b_{1s})^{1/4}} \frac{1}{[1 + k^2 \sigma^2(\theta)]^{3/2}}. \quad (\text{C8})$$

3. Optical conductivity

Focusing on the cosine term and light polarized along the x -direction, we can write

$$\Omega_{1s}^{\cos} = \frac{-2\sqrt{2\pi} i \hbar v_F}{(a_{1s} b_{1s})^{-1/4}} \int_0^{2\pi} d\theta \left[\frac{\hbar v_F \gamma(\theta) - E_g |J_\ell(\beta)| \sigma(\theta)}{E_g^2 J_\ell^2(\beta) \sigma^3(\theta) - 4\hbar^2 v_F^2 \sigma(\theta) \gamma^2(\theta)} \frac{E_g \hbar v_F |J_\ell(\beta)| \gamma(\theta) \operatorname{arccsc}\left(\frac{E_g |J_\ell(\beta)| \sigma(\theta)}{2\hbar v_F \gamma(\theta)}\right)}{(E_g^2 J_\ell^2(\beta) \sigma^2(\theta) - 4\hbar^2 v_F^2 \gamma^2(\theta))^{3/2}} \right], \quad (\text{C9})$$

where the radial integral was performed analytically, whereas the angular integral can only be worked out numerically. The term that goes with the sine leads to

$$\Omega_{1s}^{\sin} = \frac{-2\sqrt{2\pi} i \hbar v_F}{(a_{1s} b_{1s})^{-1/4}} \int_0^{2\pi} d\theta \left[\frac{-\hbar v_F \gamma(\theta)}{E_g^2 J_\ell^2(\beta) \sigma^3(\theta) - 4\hbar^2 v_F^2 \sigma(\theta) \gamma^2(\theta)} + \frac{E_g \hbar v_F |J_\ell(\beta)| \gamma(\theta) \operatorname{arccsc}\left(\frac{E_g |J_\ell(\beta)| \sigma(\theta)}{2\hbar v_F \gamma(\theta)}\right)}{(E_g^2 J_\ell^2(\beta) \sigma^2(\theta) - 4\hbar^2 v_F^2 \gamma^2(\theta))^{3/2}} \right] e^{-2i\theta_k(\beta)}, \quad (\text{C10})$$

that needs to be evaluated numerically as well. The Berry curvature is then simply $\Omega_{1s}^x = \Omega_{1s}^{\cos} + \Omega_{1s}^{\sin}$, where we put an x in the superscript to stress that the calculation was for light polarized along the x -direction. For light polarized along the y -direction, we can identify from the optical matrix element (C5) an extra factor of $J_m(\beta)$, and also a relative sign between the cosine and sine terms, so that the Berry curvature is now $\Omega_{1s}^y = J_m(\beta)(\Omega_{1s}^{\cos} - \Omega_{1s}^{\sin})$. For symmetry reasons, neither the state $2x$ nor $2y$ contribute to the optical conductivity. However, the excited state $2s$ contributes to the conductivity. Its contribution is calculated in the same way as for the $1s$ state, however, even though the radial integral can be computed analytically, its expression is quite involved, and is not relevant for the discussion. At the end, the angular integral has to be computed numerically anyway. Finally, the optical conductivity is computed through

$$\sigma_{jj}(\omega) = \frac{e^2}{8\pi^3 i \hbar} \sum_{\nu=1s,2s} \frac{E_\nu |\Omega_\nu^j|^2}{E_\nu - (\hbar\omega + i\Gamma)} + \frac{E_\nu |\Omega_\nu^j|^2}{E_\nu + \hbar\omega + i\Gamma} \quad (\text{C11})$$

where $j = x, y$ for light polarized along the x and y -directions, respectively.

Appendix D: Spatial map of the EM field

In the figure below we show a spatial map of the EM field of a TM polariton in the vicinity of the hBN mono-

layer. As one can see, the intensity of both magnetic and electric fields decay away from the 2D material located at the plane $z = 0$. We can also infer from Fig. 7 that the field in the substrate is more confined than in air. This degree of spatial confinement is in the order of the nanometers (~ 0.5 nm).

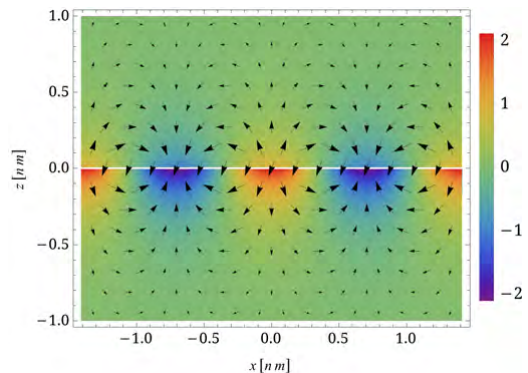


FIG. 7: Spatial map of the EM field of a TM mode. We make an intensity plot representing the intensity of the single component magnetic field, and a stream plot representing the off-plane components of electric field and respective intensities. The top half represents the field in air, while the bottom half represents the field in SiO_2 . For the frequency wavenumber pair, we picked the point in the dispersion of Fig. 5(b) of highest (real) wavenumber. This plot does not take into account the imaginary part of the wavenumber. Parameters used: $q = 4.45 \text{ nm}^{-1}$, $\hbar\omega = 5.68 \text{ eV}$, $\epsilon_1 = 1$ and $\epsilon_2 = 2.16$.

-
- [1] H. Jiang, L. Zheng, Z. Liu, and X. Wang, Two-dimensional materials: From mechanical properties to flexible mechanical sensors, *InfoMat* **2**, 1077–1094 (2020).
- [2] T. Dutta, N. Yadav, Y. Wu, G. J. Cheng, X. Liang, S. Ramakrishna, A. Sbai, R. Gupta, A. Mondal, Z. Hongyu, and A. Yadav, Electronic properties of 2D materials and their junctions, *Nano Mater. Sci.* (2023), DOI: 10.1016/j.nanoms.2023.05.003.
- [3] B. Jia, 2D optical materials and the implications for photonics, *APL Photonics* **4**, 080401 (2019).
- [4] X. Gan, K. F. Mak, Y. Gao, Y. You, F. Hatami, J. Hone, T. F. Heinz, and D. Englund, Strong enhancement of light–matter interaction in graphene coupled to a photonic crystal nanocavity, *Nano Lett.* **12**, 5626–5631 (2012).
- [5] A. K. Geim and K. S. Novoselov, The rise of graphene, *Nat. Mater.* **6**, 183–191 (2007).
- [6] J. L. Miller, A family of two-dimensional conductors comes into bloom, *Phys. Today* **76**(6), 12 (2023).
- [7] X. Song, J. Hu, and H. Zeng, Two-dimensional semiconductors: recent progress and future perspectives, *J. Mater. Chem. C* **1**, 2952–2969 (2013).
- [8] X. Huang, C. Liu, and P. Zhou, 2D semiconductors for specific electronic applications: from device to system, *npj 2D Mater. Appl.* **6**, 51 (2022).
- [9] Y. Cao, D. Chowdhury, D. Rodan-Legrain, O. Rubies-Bigorda, K. Watanabe, T. Taniguchi, T. Senthil, and P. Jarillo-Herrero, Strange metal in magic-angle graphene with near Planckian dissipation, *Phys. Rev. Lett.* **124**, 076801 (2020).
- [10] Z. Jiang, P. Wang, X. Jiang, and J. Zhao, MBene (MnB): a new type of 2D metallic ferromagnet with high Curie temperature, *Nanoscale Horiz.* **3**, 335–341 (2018).
- [11] S. Yu, X. Li, J. Tang, Y. Wang, F. Xu, and X. Wang, Recent advances in two-dimensional ferromagnetism: strain-, doping-, structural- and electric field-engineering toward spintronic applications, *Sci. Technol. Adv. Mater.* **23**, 140–160 (2022).
- [12] D. Qiu, C. Gong, S. Wang, M. Zhang, C. Yang, X. Wang, and J. Xiong, Recent advances in 2D superconductors, *Adv. Mater.* **33**, 2006124 (2021).
- [13] Y. Cao, V. Fatemi, S. Fang, K. Watanabe, T. Taniguchi, E. Kaxiras, and P. Jarillo-Herrero, Unconventional superconductivity in magic-angle graphene superlattices, *Nature* **556**, 43–50 (2018).
- [14] J. M. Park, Y. Cao, K. Watanabe, T. Taniguchi, and P. Jarillo-Herrero, Tunable strongly coupled superconductivity in magic-angle twisted trilayer graphene, *Nature* **590**, 249–255 (2021).

- [15] Y. Cao, V. Fatemi, A. Demir, S. Fang, S. L. Tomarken, J. Y. Luo, J. D. Sanchez-Yamagishi, K. Watanabe, T. Taniguchi, E. Kaxiras, R. C. Ashoori, and P. Jarillo-Herrero, Correlated insulator behaviour at half-filling in magic-angle graphene superlattices, *Nature* **556**, 80–84 (2018).
- [16] I. H. Abidi, N. Mendelson, T. T. Tran, A. Tyagi, M. Zhuang, L.-T. Weng, B. Özyilmaz, I. Aharonovich, M. Toth, and Z. Luo, Selective defect formation in hexagonal boron nitride, *Adv. Opt. Mater.* **7**, 1900397 (2019).
- [17] L. Banszerus, M. Schmitz, S. Engels, M. Goldsche, K. Watanabe, T. Taniguchi, B. Beschoten, and C. Stampfer, Ballistic transport exceeding 28 μm in CVD grown graphene, *Nano Lett.* **16**, 1387–1391 (2016).
- [18] D. J. Rizzo, J. Zhang, B. S. Jessen, F. L. Ruta, M. Cothrine, J. Yan, D. G. Mandrus, S. E. Nagler, T. Taniguchi, K. Watanabe, M. M. Fogler, A. N. Papsupathy, A. J. Millis, A. Rubio, J. C. Hone, C. R. Dean, and D. N. Basov, Polaritonic probe of an emergent 2D dipole interface, *Nano Lett.* **23**, 8426–8435 (2023).
- [19] C. Elias, P. Valvin, T. Pelini, A. Summerfield, C. J. Mellor, T. S. Cheng, L. Eaves, C. T. Foxon, P. H. Beton, S. V. Novikov, B. Gil, and G. Cassabois, Direct band-gap crossover in epitaxial monolayer boron nitride, *Nat. Commun.* **10**, 2639 (2019).
- [20] W. Yang, L. K. Ang, W. Zhang, J. Han, and Y. Xu, High sensitivity gas sensor based on surface exciton polariton enhanced photonic spin Hall effect, *Opt. Express* **31**, 27041–27053 (2023).
- [21] S. Li, A. Pershin, G. Thiering, P. Udvarhelyi, and A. Gali, Ultraviolet quantum emitters in hexagonal boron nitride from carbon clusters, *J. Phys. Chem. Lett.* **13**, 3150–3157 (2022).
- [22] A. K. Geim and I. V. Grigorieva, Van der Waals heterostructures, *Nature* **499**, 419 (2013).
- [23] J. C. G. Henriques, B. Amorim, R. M. Ribeiro, and N. M. R. Peres, Excitonic response of AA' and AB stacked hBN bilayers, *Phys. Rev. B* **105**, 115421 (2022).
- [24] E. V. Castro, K. S. Novoselov, S. V. Morozov, N. M. R. Peres, J. M. B. L. dos Santos, J. Nilsson, F. Guinea, A. K. Geim, and A. H. C. Neto, Biased bilayer graphene: Semiconductor with a gap tunable by the electric field effect, *Phys. Rev. Lett.* **99**, 216802 (2007).
- [25] R. Bistritzer and A. H. MacDonald, Moiré bands in twisted double-layer graphene, *Proc. Nat. Acad. Sci. U. S. A.* **108**, 12233–12237 (2011).
- [26] J. M. B. Lopes dos Santos, N. M. R. Peres, and A. H. Castro Neto, Graphene bilayer with a twist: Electronic structure, *Phys. Rev. Lett.* **99**, 256802 (2007).
- [27] Z. Hennighausen and S. Kar, Twistronics: a turning point in 2D quantum materials, *Electron. Struct.* **3**, 014004 (2021).
- [28] A. Chaves, J. G. Azadani, H. Alsalman, D. R. da Costa, R. Frisenda, A. J. Chaves, S. H. Song, Y. D. Kim, D. He, J. Zhou, A. Castellanos-Gomez, F. M. Peeters, Z. Liu, C. L. Hinkle, S.-H. Oh, P. D. Ye, S. J. Koester, Y. H. Lee, P. Avouris, X. Wang, and T. Low, Bandgap engineering of two-dimensional semiconductor materials, *npj 2D Mater. Appl.* **4**, 29 (2020).
- [29] L. Xue, S. Liu, Y. Hang, A. M. Summers, D. J. Wilson, X. Wang, P. Chen, T. G. Folland, J. A. Hachtel, H. Shi, S. Hosseini-Zavareh, S. R. Das, S. Lei, Z. Zhang, C. M. Sorensen, W. Guo, J. D. Caldwell, J. H. Edgar, C. I. Blaga, and C. A. Trallero-Herrero, Unraveling ultrafast photoionization in hexagonal boron nitride, arXiv:2101.10429.
- [30] K. S. Thygesen, Calculating excitons, plasmons, and quasiparticles in 2D materials and van der Waals heterostructures, *2D Materials* **4**, 022004 (2017).
- [31] A. Bhattacharya, S. Bhattacharya, and G. P. Das, Band gap engineering by functionalization of BN sheet, *Phys. Rev. B* **85**, 035415 (2012).
- [32] R. J. P. Román, F. J. R. C. Costa, A. Zobelli, C. Elias, P. Valvin, G. Cassabois, B. Gil, A. Summerfield, T. S. Cheng, C. J. Mellor, P. H. Beton, S. V. Novikov, and L. F. Zagonel, Band gap measurements of monolayer h-BN and insights into carbon-related point defects, *2D Materials* **8**, 044001 (2021).
- [33] F. Ferreira, A. J. Chaves, N. M. R. Peres, and R. M. Ribeiro, Excitons in hexagonal boron nitride single-layer: a new platform for polaritonics in the ultraviolet, *J. Opt. Soc. Am. B* **36**, 674–683 (2019).
- [34] K. P. Fears, D. Y. Petrovykh, S. J. Photiadis, and T. D. Clark, Circular dichroism analysis of cyclic β -helical peptides adsorbed on planar fused quartz, *Langmuir* **29**, 10095–10101 (2013).
- [35] A. H. Castro Neto, F. Guinea, N. M. R. Peres, K. S. Novoselov, and A. K. Geim, The electronic properties of graphene, *Rev. Mod. Phys.* **81**, 109 (2009).
- [36] C.-H. Park, L. Yang, Y.-W. Son, M. L. Cohen, and S. G. Louie, New generation of massless Dirac fermions in graphene under external periodic potentials, *Phys. Rev. Lett.* **101**, 126804 (2008).
- [37] M. F. C. M. Quintela, J. C. G. Henriques, L. G. M. Tenório, and N. M. R. Peres, Theoretical methods for excitonic physics in 2D materials, *phys. stat. solid. (b)* **259**, 2200097 (2022).
- [38] J. Have, G. Catarina, T. G. Pedersen, and N. M. R. Peres, Monolayer transition metal dichalcogenides in strong magnetic fields: Validating the Wannier model using a microscopic calculation, *Phys. Rev. B* **99**, 035416 (2019).
- [39] J. N. S. Gomes, C. Trallero-Giner, and M. I. Vasilevskiy, Variational calculation of the lowest exciton states in phosphorene and transition metal dichalcogenides, *J. Phys.: Cond. Matter* **34**, 045702 (2021).
- [40] M. F. C. Martins Quintela and N. M. R. Peres, A colloquium on the variational method applied to excitons in 2D materials, *Eur. Phys. J. B* **93**, 222 (2020).
- [41] J. C. G. Henriques, N. A. Mortensen, and N. M. R. Peres, Analytical description of the 1s exciton linewidth temperature dependence in transition metal dichalcogenides, *Phys. Rev. B* **103**, 235402 (2021).
- [42] J. J. Sakurai and J. Napolitano, *Modern Quantum Mechanics*, 3rd ed. (Cambridge University Press, 2020).
- [43] T. G. Pedersen, Intraband effects in excitonic second-harmonic generation, *Phys. Rev. B* **92**, 235432 (2015).
- [44] J. C. G. Henriques, G. B. Ventura, C. D. M. Fernandes, and N. M. R. Peres, Optical absorption of single-layer hexagonal boron nitride in the ultraviolet, *J. Phys.: Cond. Matter* **32**, 025304 (2019).
- [45] Y. V. BLudov, A. Ferreira, N. M. R. Peres, and M. I. Vasilevskiy, A primer on surface plasmon-polaritons in graphene, *Int. J. Mod. Phys. B* **27**, 1341001 (2013).
- [46] L. Ju, L. Wang, T. Cao, T. Taniguchi, K. Watanabe, S. G. Louie, F. Rana, J. Park, J. Hone, F. Wang, and P. L. McEuen, Tunable excitons in bilayer graphene, *Sci-*

- ence **358**, 907–910 (2017).
- [47] J. C. G. Henriques, I. Epstein, and N. M. R. Peres, Absorption and optical selection rules of tunable excitons in biased bilayer graphene, *Phys. Rev. B* **105**, 045411 (2022).
- [48] D. N. Basov, A. Asenjo-Garcia, P. J. Schuck, X. Zhu, and A. Rubio, Polariton panorama, *Nanophotonics* **10**, 549 (2021).
- [49] P. A. D. Gonçalves and N. M. R. Peres, *An Introduction to Graphene Plasmonics* (World Scientific, Singapore, 2016).
- [50] N. V. Leppenen, L. E. Golub, and E. L. Ivchenko, Sommerfeld enhancement factor in two-dimensional Dirac materials, *Phys. Rev. B* **103**, 235311 (2021).
- [51] C. Wolff, K. Busch, and N. A. Mortensen, Modal expansions in periodic photonic systems with material loss and dispersion, *Phys. Rev. B* **97**, 104203 (2018).
- [52] B. P. van Zyl and E. Zaremba, Thomas–Fermi–Dirac–von Weizsäcker hydrodynamics in laterally modulated electronic systems, *Phys. Rev. B* **59**, 2079 (1999).
- [53] V. Fessatidis and H. L. Cui, Hydrodynamic theory of magnetoplasmons in a modulated two-dimensional electron gas, *Phys. Rev. B* **43**, 11725 (1991).
- [54] Y. Chu, L. Liu, Y. Yuan, C. Shen, R. Yang, D. Shi, W. Yang, and G. Zhang, A review of experimental advances in twisted graphene moiré superlattice, *Chin. Physics B* **29**, 128104 (2020).
- [55] W. Yan, L. Meng, Z. Meng, Y. Weng, L. Kang, and X.-a. Li, Probing angle-dependent interlayer coupling in twisted bilayer WS₂, *J. Phys. Chem. C* **123**, 30684–30688 (2019).
- [56] H. Y. Lee, M. M. Al Ezzi, N. Raghuvanshi, J. Y. Chung, K. Watanabe, T. Taniguchi, S. Garaj, S. Adam, and S. Gradečak, Tunable optical properties of thin films controlled by the interface twist angle, *Nano Lett.* **21**, 2832–2839 (2021).
- [57] S. Brem and E. Malic, Bosonic delocalization of dipolar moiré excitons, *Nano Lett.* **23**, 4627–4633 (2023).
- [58] P. Roman-Taboada, E. Obregon-Castillo, A. R. Botello-Mendez, and C. Noguez, Excitons in twisted aa′ hexagonal boron nitride bilayers, *Phys. Rev. B* **108**, 075109 (2023).
- [59] T. Stauber and H. Kohler, Quasi-flat plasmonic bands in twisted bilayer graphene, *Nano Lett.* **16**, 6844–6849 (2016).
- [60] B. Wu, H. Zheng, S. Li, J. Ding, J. He, Y. Zeng, K. Chen, Z. Liu, S. Chen, A. Pan, and Y. Liu, Evidence for moiré intralayer excitons in twisted WSe₂/WSe₂ homobilayer superlattices, *Light Sci. Appl.* **11**, 166 (2022).
- [61] S. Zhao, Z. Li, X. Huang, A. Rupp, J. Göser, I. A. Vovk, S. Y. Kruchinin, K. Watanabe, T. Taniguchi, I. Bilgin, A. S. Baimuratov, and A. Högele, Excitons in mesoscopically reconstructed moiré heterostructures, *Nat. Nanotechnol.* **18**, 572–579 (2023).
- [62] N. W. Ashcroft and N. D. Mermin, *Solid State Physics* (Harcourt, Orlando, 1976).
- [63] C.-H. Park, L. Yang, Y.-W. Son, M. L. Cohen, and S. G. Louie, Anisotropic behaviours of massless Dirac fermions in graphene under periodic potentials, *Nat. Phys.* **4**, 213–217 (2008).